Noname manuscript No.
(will be inserted by the editor)

Hele-Shaw Beach Creation by Breaking Waves

A mathematics-inspired experiment

Anthony Thornton · Avraham van der Horn · Wout Zweers · Devaraj van der Meer · Onno Bokhove

Received: date / Accepted: date

Abstract Fundamentals of nonlinear wave-particle interactions are studied in a Hele-Shaw configuration with wave breaking and a dynamic bed. To design this configuration, we determine, mathematically, the gap width which allows inertial flows to survive the viscous damping due to the side walls. Damped wave sloshing experiments compared with simulations confirm that width-averaged potential-flow models with linear momentum damping are adequately capturing the large scale nonlinear wave motion. Subsequently, we show that the four types of wave breaking on real-world beaches also emerge on Hele-Shaw laboratory beaches, albeit in idealized forms. Finally, an experimental parameter study is undertaken to quantify the formation of quasi-steady beach morphologies due to nonlinear, breaking waves: berm or dune, beach and sandbar formation are all classified. Our research reveals that the

We acknowledge technical assistance from Gert-Wim Bruggert, and financial support from the MultiScale Mechanics and Physics of Fluids groups of Stefan Luding and Detlef Lohse (University of Twente), respectively, as well as the Stichting Free Flow Foundation (O.B., Twente/Leeds).

A.R. Thornton
Department of Mechanical Engineering, University of Twente, Enschede, The Netherlands
E-mail: a.r.thornton@utwente.nl

A.J. van der Horn
Department of Physics, University of Twente, Enschede, The Netherlands

D. van der Meer
Department of Physics, University of Twente, Enschede, The Netherlands
E-mail: d.vandermeer@utwente.nl

W. Zweers
FabLab Saxion Hogeschool, Enschede, The Netherlands
E-mail: zweers@dds.nl

O. Bokhove
School of Mathematics, University of Leeds, LS2 9JT, Leeds, United Kingdom
Department of Applied Mathematics, University of Twente, Enschede, The Netherlands
E-mail: o.bokhove@leeds.ac.uk

Hele-Shaw beach configuration allows a wealth of experimental and modelling extensions, including benchmarking of forecast models used in the coastal engineering practice.

Keywords Hele-Shaw cell · laboratory experiments · mathematical design · potential flow and shallow water simulations

1 Introduction

1.1 A slice of beach

Natural beaches, as well as those which are partially enhanced or even completely man-made, are defensive zones that protect large tracts of the world's coastlines against storm surges. This is especially the case in low-lying deltas such as the western and northern parts of The Netherlands, with its combination of a partially and totally reinforced coastline of beaches and dunes, and dikes. The dynamics of the surf zone, concerning the wet zone from the beach to the offshore line where the white capping of wave breaking starts, are very important for understanding how beaches, berms and sand banks form and erode. Good predictions of surf zone dynamics and the associated sand transport can reveal where sand suppletion will be required to protect the coast, or where dredging is needed to keep navigational inlets into harbours open.

Coastal engineers and fluid dynamicists have made great progress in formulating models for waves and currents, and sand transport in and around the surf zone. This progress has provided the fundamentals for operational forecast models such as Telemac, Delft-3D and Xbeach [22]. Current forecast models are founded on decades of research on wave dynamics and beach erosion, especially during storms [24; 20], on the formulation of the sediment and bedload flux transport laws [26; 8; 11; 19], and on direct mathematical analysis [15]. Despite great advances, the fundamental laws of how sand is picked up, transported and deposited by breaking waves remain relatively poorly understood at a fundamental level. The key issues are how to grasp and simplify the complex interactions in the multiphase fluid and solid dynamics of air, (salt) water and sand particles. This gap in knowledge motivates the larger goal of our research: demonstrating how a novel, compact Hele-Shaw beach configuration and laboratory experiment can shed new light on fundamental issues.

The wave breaking process is comprised of complicated two-phase hydrodynamics of water and air, and three-phase flows through its interaction with suspended sediment and the sand bottom. To facilitate a combined modelling and experimental effort, we focus our investigations on the fundamental aspects of sand transport by breaking waves. This emphasis has been realised by simplifying some aspects of the challenge via a reduction of the degrees of freedom involved. Practically, we investigate the dynamics in a slice of beach: a thin vertical layer of water, air and sand particle bottom. Hence, the dynamics is made nearly two-dimensional, which effects the reduced degrees of freedom

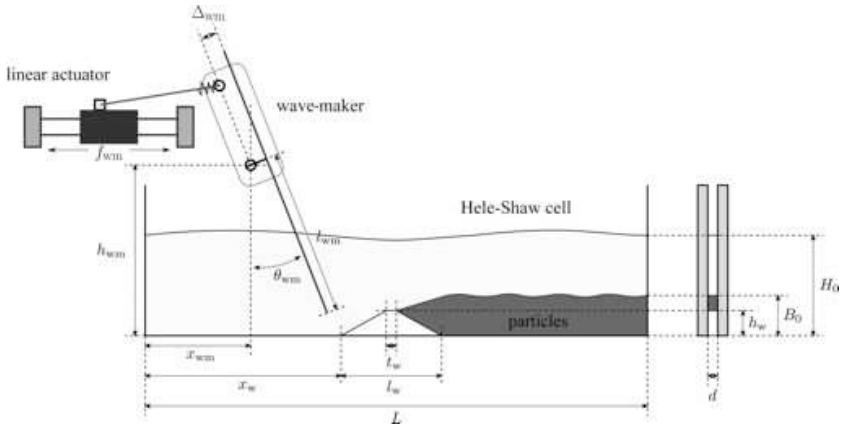

Fig. 1 A schematic front and side view of the Hele-Shaw beach experiment is sketched. Parameters indicated are defined (later) in the text. The wedge ensures that the particles of the beach on the right remain separate from the wave-maker region on the left.

mentioned. In nature, such a slice of beach would be a few sand particles thin, tens of meters long and one to a few meters in depth. Instead, this slice of natural beach is scaled down to table-top size, resulting into a Hele-Shaw set-up of about one metre long, a few millimetres wide, and up and about 30cm in height [5]. A sketch of the set-up between two vertical glass plates with closed sides and bottom is provided in Fig. 1. The Hele-Shaw beach is a novel adaptation of the classical Hele-Shaw cell, e.g., the one concerning single fluid flow around solid obstacles [18]. The dynamics in this renewed Hele-Shaw cell takes effectively place in a vertical plane such that gravity is the restoring force permitting surface wave motion. The tank is filled with nearly spherical, zeolite or glass particles and water, and is open at the top. Instead of wind-driven waves or swell travelling onshore, the waves are mechanically driven by a programmable wave-maker; an inverted pendulum or rod fit loosely between the two glass plates. In the next subsection, we present some precursory results, and show that the phenomena of wave breaking and beach formation are captured reasonably well within the Hele-Shaw beach configuration.

1.2 Precursory results and goals

The principal drawback of the Hele-Shaw beach set-up is the proximity of the glass plates because they can lead to heavy damping of the momentum due to a Poisseuille-type lateral flow profile, dominated by viscous effects [18]. To assess these viscous effects, some mathematical analysis of the hydrodynamic equations was undertaken before any design or testing [5; 6] commenced. This analysis was aimed at determining the minimal threshold gap width between the glass plates at which juncture a breaking wave or bore, generated at the offshore end of the tank, would become damped out at the other, onshore

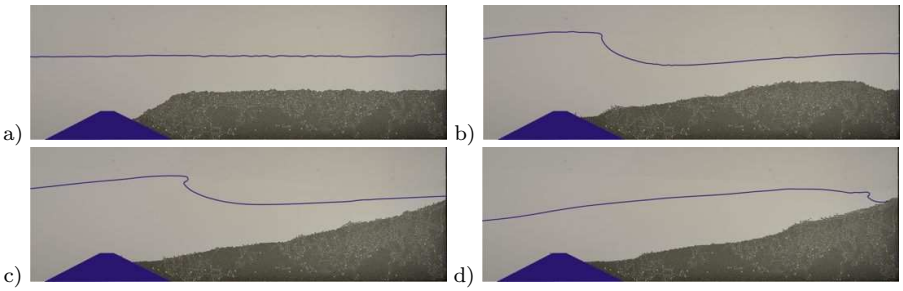

Fig. 2 Beach formation by breaking waves. a) The initial state is shown before the wavemaker (not shown) starts. b) Waves move material from behind the wedge onshore, c) such that over time a beach with nearly constant slope forms on the right (note the spilling breaker). d) The final quasi-steady state has a dry beach (note the surging breaker). Particle bed in grey. Waves come from the left. Water line and wedge have been highlighted in blue.

end of the tank, given a fixed beach bathymetry. Consequently, the first goal of the paper is to present the mathematics that inspired the design of the experiment. The design consists of width- and depth-averaging the Navier-Stokes equations, which assumes suitable velocity profiles, that in turn yield two systems of simplified flow equations: the incompressible Euler equations with linear momentum damping in two dimensions and the shallow water equations in one spatial dimension. Simulation of this shallow system allows us to calculate an optimal gap width. Using a potential flow Ansatz, we further simplify our damped Euler equations in two dimensions to damped water wave equations. Through mathematical analysis and simulations, solutions of these water wave equations will subsequently be validated against preliminary laboratory experiments of wave sloshing in the Hele-Shaw set-up, in the absence of particles. The latter validation experiments are geared to address the question:

(i) to what extent does the linear momentum damping constitute the primary energy dissipation mechanism in the Hele-Shaw set-up?

The primary advantage of the Hele-Shaw beach configuration is that everything becomes clearly visible: the dynamics of each particle, as well as the free surface motion, can be traced accurately in time. The configuration is of interest both experimentally and theoretically, as it renders mathematical and numerical modelling significantly more feasible than the present modelling of surf zone dynamics at real-world beaches. Although the gap width can be adjusted to become one$^+$ to a few particle diameters in width, we presently limit ourselves to a gap width of circa 1.1 particle diameter. Only a few thousand particles —a few spoonfulls— are involved in the set-up.

All wave types classified in the coastal engineering and fluid dynamics literature [3; 23] are identifiable in the Hele-Shaw beach cell. The classification involves spilling, plunging, collapsing and surging breakers, which range, in order of appearance, from steep waves on mild slopes to low, shallow waves on steep slopes, see Fig. 2(c,d). These waves cause weak or no reflection to strong

reflection, respectively. In the literature [3], a distinction of the four wave types above is based on the Iribarren number, $I_b = \tan\alpha/\sqrt{H_b/L_b}$, which relates the beach slope $\tan\alpha$ at wave breaking with the square root of the ratio of the breaker wave height H_b and the (deep-water) wave length L_b. Although not set in stone, the ranges are roughly $I_b > 3.3$, $2.0 < I_b < 3.3$, $0.4 < I_b < 2.0$ and $I_b < 0.4$ for surging, collapsing, plunging and spilling breakers. Our second goal is therefore to address the question:

(ii) how do the types of wave breakers waves observed in the Hele-Shaw cell relate to those observed at outside beaches?

The variety of wave breakers observed is intimately related to the evolving bathymetry. While the wave motion favouring bed evolution in the experiment occurs on frequencies of around 1Hz, bed evolution occurs on longer time scales of minutes to an hour. An example of beach evolution is provided in Fig. 2. Although the set-up allows for a range of liquid densities, particles sizes, and wave-maker frequencies to be varied, uniformly or non-uniformly, we limit the investigation to variation of three basic parameters: the monochromatic wave-maker frequency f_{wm}, the still water bed level B_0 and the still water level H_0, for monodispersed nearly spherical particles. For definitions see Fig. 1. The final question we wish to address thus becomes:

(iii) what stable quasi-steady beach morphologies will be observed in the Hele-Shaw beach set-up as function of the parameters f_{wm}, B_0 and H_0?

The mathematical design question and three questions posed above yield the following outline. In section 2, the mathematical design is presented. The experimental set-up and techniques are explained in section 3. The laboratory results on breaking waves are disseminated in section 4. The quasi-steady beach morphologies and their classification are analysed in detail in section 5. Finally, we conclude in section 6.

2 Mathematics of experimental design

The primary goal of this section is to determine the threshold gap width for which a broken wave can propagate from one end of the tank to the other, without diminishing due to the side wall friction. Waves generated at one end of the tank usually break usually when they reach the shallow region behind the wedge which holds back particles from the wave-maker region. The relevant dimensions concern a tank of a half to one metre in length and with a still water depth H_0 of about 0 to 10 centimetres. The strategy is to simplify the Navier-Stokes equations of motion for a fixed beach of gentle slope that remains dry onshore. The steps in the derivation are as follows:

– Scale the equations given the anisotropy of lateral, zonal and depth scales of space and velocity. Then average the Navier-Stokes equations laterally assuming a Poisseuille-type flow profile across the gap following the adopted scaling.

– Subsequently, average the resulting planar, incompressible Euler equations with linear momentum damping across the depth, assuming hydrostatic balance to hold. To determine the threshold gap width, simulations of the resulting shallow water equations are performed for suitable wave forcing.
– Additionally, these planar Euler equations are simplified further using a potential flow Ansatz. The energy balance in the resulting potential flow water wave equations is then analysed theoretically for experimental use.

Our analysis begins with the incompressible Navier-Stokes equations for a homogeneous fluid, i.e.,

$$\partial_t u + u\partial_x u + v\partial_y u + w\partial_z u = -\frac{1}{\rho_0}\partial_x p + \nu\big(\partial_x^2 + \partial_y^2 + \partial_z^2\big)u, \tag{1a}$$

$$\partial_t v + u\partial_x v + v\partial_y v + w\partial_z v = -\frac{1}{\rho_0}\partial_y p + \nu\big(\partial_x^2 + \partial_y^2 + \partial_z^2\big)v, \tag{1b}$$

$$\partial_t w + u\partial_x w + v\partial_y w + w\partial_z w = -\frac{1}{\rho_0}\partial_z p - g + \nu\big(\partial_x^2 + \partial_y^2 + \partial_z^2\big)w, \tag{1c}$$

$$\partial_x u + \partial_y v + \partial_z w = 0, \tag{1d}$$

in which partial derivatives $\partial_t(\cdot) = \partial(\cdot)/\partial_t$, $\partial_y^2(\cdot) = \partial^2(\cdot)/\partial_y^2$, and so forth; velocity field (u, v, w) and pressure p are functions of spatial coordinares $(x, y, z)^T$ and time t, $\rho_0 = 998\text{kg/m}^3$ is the constant fluid density, $g = 9.8\text{m/s}^2$ the Earth's acceleration vector and $\nu = 10^{-6}\text{m}^2/\text{s}$ the kinematic viscosity.

2.1 Width and depth averaging

First, all dimensional coordinates and variables will be denoted with as superscript a star. Second, coordinates and variables in (1) are made non-dimensional as follows:

$$u^\star = Uu, \quad v^\star = Vv, \quad w^\star = Ww, \quad x^\star = Lx, \quad y^\star = ly, \quad z^\star = Dz, \tag{2a}$$

$$t^\star = Tt, \quad p^\star = P_0 p \tag{2b}$$

with the starred dimensional variables and coordinates just introduced. The time scale $T \approx L/U \approx l/V \approx D/W$, and pressure scale $P_0 = \rho_0 U^2/(Re\,\epsilon^2)$ with Reynolds number $Re = UL/\nu$, Froude number $1/Fr^2 = gD/U^2$, and aspect ratios $\epsilon = l/L \ll 1$ and $\delta = D/L$. Upon substitution and rearranging, the resulting non-dimensional equations become:

$$\partial_t u + u\partial_x u + v\partial_y u + w\partial_z u = -\frac{1}{Re\,\epsilon^2}\partial_x p + \frac{1}{Re}\big(\partial_x^2 + \frac{1}{\epsilon^2}\partial_y^2 + \frac{1}{\delta^2}\partial_z^2\big)u \tag{3a}$$

$$\partial_t v + u\partial_x v + v\partial_y v + w\partial_z v = -\frac{1}{Re\,\epsilon^4}\partial_y p + \frac{1}{Re}\big(\partial_x^2 + \frac{1}{\epsilon^2}\partial_y^2 + \frac{1}{\delta^2}\partial_z^2\big)v \tag{3b}$$

$$\partial_t w + u\partial_x w + v\partial_y w + w\partial_z w = -\frac{1}{Re\,\epsilon^2\,\delta^2}\partial_z p - \frac{1}{Fr^2\delta^2} + \frac{1}{Re}\big(\partial_x^2 + \frac{1}{\epsilon^2}\partial_y^2 + \frac{1}{\delta^2}\partial_z^2\big)w \tag{3c}$$

$$\partial_x u + \partial_y v + \partial_z w = 0. \tag{3d}$$

The Reynolds number is about $Re = 10^3$ to 10^4 and $\epsilon^2 = 4\times10^{-4}$ for $U = 0.01$ to 0.1m/s, $L = 0.1$m and $l = 2 \times 10^{-3}$m, such that $Re\,\epsilon^2 \approx 1$. While the two tanks used are about 0.6m and 1m long, the typical length scale of the phenomena generated is smaller, about $L = 0.1$m, in part also because the wave-maker is placed at about $1/3^{\text{rd}}$ of the tank's length. We will generate waves in the set-up using a sinusoidally-driven wave-maker. Essentially, an upper limit for U follows from the wave-maker motion as

$$U = 2\pi f_{wm}\theta_{wm}l_{wm} = \mathcal{O}\,(0.1)\,\text{m/s} \tag{4}$$

with wave-maker frequency $f_{wm} \approx 1.3$Hz, wave-maker angle $\theta_{wm} \approx 20^\circ = 1/9\,\text{rad}$ and wave-maker arm $l_{wm} \approx 0.32$m. Clearly at leading order in ϵ^2 the lateral momentum equation in (3) yields $p = p(x, z, t)$ to be y–independent. Hence, only the viscous contribution in the lateral direction remains of importance in the zonal and vertical momentum equations. With this simplification, the reduced equations read

$$\partial_t u + u\partial_x u + v\partial_y u + w\partial_z u = -\frac{1}{Re\,\epsilon^2}\partial_x p + \frac{1}{Re\epsilon^2}\partial_y^2 u, \tag{5a}$$

$$\partial_t w + u\partial_x w + v\partial_y w + w\partial_z w = -\frac{1}{Re\,\epsilon^2\,\delta^2}\partial_z p - \frac{1}{Fr^2\delta^2} + \frac{1}{Re\,\epsilon^2}\partial_y^2 w, \tag{5b}$$

$$\partial_x u + \partial_y v + \partial_z w = 0. \tag{5c}$$

It is tempting to assume a balance between pressure gradients and the remaining viscous terms, such that dimensionally

$$u^\star = -\frac{1}{2\rho_0\nu}\partial_{x^\star}p^\star(l^2 - y_\star^2) \quad \text{and} \quad w^\star = -\frac{1}{2\rho_0\nu}(\partial_{z^\star}p^\star + \rho_0 g)\,(l^2 - y_\star^2). \tag{6}$$

A comparison between the magnitude of the inertia terms $\rho_0 Du_\star/Dt \sim \rho_0(u_\star^2 + w_\star^2)/L$ over the pressure gradient $|\boldsymbol{\nabla}_{x^\star z^\star}p^\star|$ or viscous terms (e.g., [2]), using hydrostatic balance to estimate the pressure gradient (see below), yields

$$\begin{aligned}\frac{\rho_0(u_\star^2 + w_\star^2)}{L|\nabla_{x^\star z^\star}p^\star|}\,\frac{16l^4|\nabla_{x^\star z^\star}p^\star|}{\rho_0\nu^2L^2} &= \frac{16l^4 g\Delta h}{\nu^2L^2}\\ &= \frac{16\,10^{-12}\times 10\times 10^{-2}}{10^{-12}\times(0.1, 0.5)^2} \sim 1 \text{ to } 100.\end{aligned} \tag{7}$$

Consequently, inertial terms remain of importance, and there is no global Hele-Shaw flow despite the narrowness of the set-up.

Pohlhausen [25] suggested to substitute the quadratic approximation

$$u = \frac{3}{2}\bar{u}\frac{(l^2 - y^2)}{l^2} \qquad \text{and} \qquad w = \frac{3}{2}\bar{w}\frac{(l^2 - y^2)}{l^2} \tag{8}$$

based on substituting the balance (6) into (5) and then laterally averaging these equations, using a width average $\bar{u} = \int_{-l}^{l} u(x, y, z, t)\mathrm{d}y/(2l)$, etc. For clarity, we keep l as a place holder, even though in the dimensionless case $l = 1$. Wilson and Duffy [27] showed this approximation to be rather good in a

similar yet different lubrication application, in a comparison with a numerical solution of the Navier-Stokes equations. The Ansatz (8) could also be viewed as a simple numerical discretization of u and w in the y-direction. The width-averaging step is followed by a simplification that sets the average of products or functions equal to the product or function of the averages, thus neglecting (Reynolds) stress terms. The resulting system of two-dimensional equations in dimensional form (dropping the stars) reads

$$\partial_t \bar{u} + \gamma \bar{u} \partial_x \bar{u} + \gamma \bar{w} \partial_z \bar{u} = -\frac{1}{\rho_0} \partial_x P - 3\nu \bar{u}/l^2, \tag{9a}$$

$$\partial_t \bar{w} + \gamma \bar{u} \partial_x \bar{w} + \gamma \bar{w} \partial_z \bar{w} = -\frac{1}{\rho_0} \partial_z P - g - 3\nu \bar{w}/l^2, \tag{9b}$$

$$\partial_x \bar{u} + \partial_z \bar{w} = 0, \tag{9c}$$

where a y–independent pressure $P = P(x, z, t)$ and $\gamma = 6/5$ for the quadratic Pohlhausen lateral flow profile are used. The kinematic free surface and bottom boundary conditions required at $z = h(x,t) + b(x,t)$ and $z = b(x,t)$ with water depth $h = h(x,t)$ and bottom height $b = b(x,t)$ are as follows

$$\partial_t (h+b) + \bar{u} \partial_x (h+b) - \bar{w} = 0 \qquad \text{at} \quad z = h(x,t) + b(x,t), \tag{10a}$$

$$\partial_t b + \bar{u} \partial_x b - \bar{w} = 0 \qquad \text{at} \quad z = b(x,t), \tag{10b}$$

at the moment for a given function $b(x,t)$.

The next, classical step is to use the anisotropy in the horizontal and vertical directions and average over depth while using hydrostatic balance. Hydrostatic balance emerges in the limit $\delta \to 0$ from (5), in non-dimensional terms as $\partial_z p/(Re\,\epsilon^2) + 1/Fr^2 = 0$, or dimensionally as

$$\partial_{z^\star} P^\star/\rho_0 + g = 0. \tag{11}$$

Integration of hydrostatic balance from a level z in the fluid to the free surface yields $P(x,z,t) = \rho_0 g\big(h(x,t) + b(x,t) - z\big)$. The estimate of the horizontal pressure gradient used above in (7) thus becomes $\rho_0 \Delta h/L$. After depth averaging and again neglecting (other Reynolds) stress terms, assuming a uniform flow profile over depth, damped shallow water equations emerge

$$\partial_t (h\bar{\bar{u}}) + \partial_x \big(\gamma h \bar{\bar{u}}^2 + g h^2/2\big) = -gh\partial_x b + (\gamma - 1)\bar{\bar{u}} \partial_x (h\bar{\bar{u}}) - 3\nu h \bar{\bar{u}}/l^2 \tag{12a}$$

$$\partial_t h + \partial_x (h\bar{\bar{u}}) = 0 \tag{12b}$$

with $h\bar{\bar{u}}(x,t) = \int_b^{h+b} \bar{u}(x,z,t)\mathrm{d}z$. These shallow water equations are augmented with hydraulic jump and bore relations to allow for local discontinuities in the depth and velocity. These jumps hold at isolated points in the horizontal. They are models for breaking waves such that mass and momentum are conserved, but the total energy is not. Integration of (12) across the discontinuity in space, or in space-time, immediately leads to the desired hydraulic jump relations. For simplicity we take $\gamma = 1$ to reduce matters to the

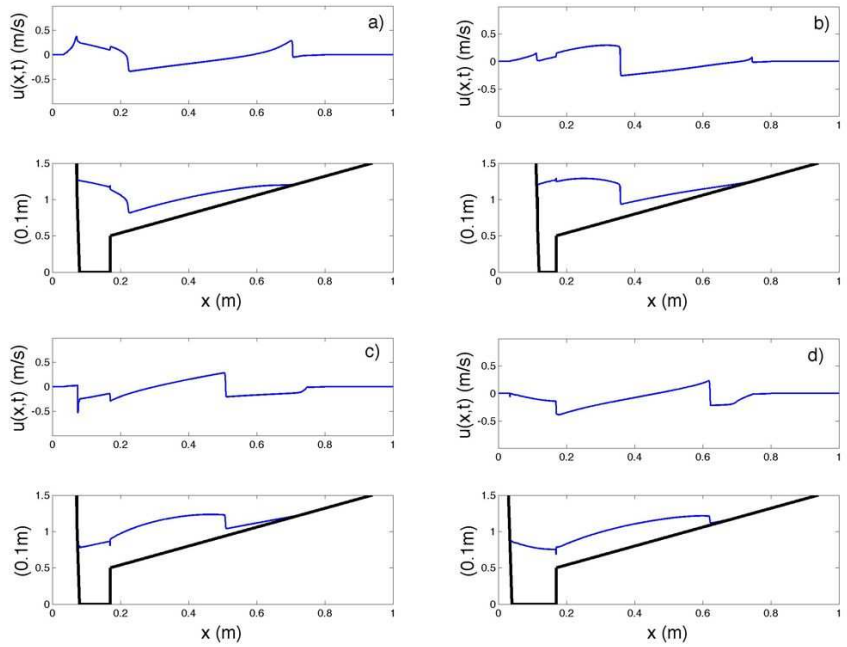

Fig. 3 The design is based on simulations of shallow-water bore propagation in the Hele-Shaw cell, illustrated here by snapshots of depth-averaged velocity $u(x,t)$, topography $b(x,t)$ (black, fat line) and free surface $h+b(x,t)$ (blue, normal line), for a gap width of $l = 1$mm. On the left, a wave-maker is modelled as a steep, moving wall with fixed $\partial_x b(x,t) < 0$, to the right of which the topography $b(x)$ is fixed. a) $t = 3.25T$, b) $t = 3.5T$, c) $t = 3.75T$, and d) $t = 4.0T$ with period $T = 1$s.

standard shallow water equations. Given a discontinuity at $x = x_b(t)$ the bore speed $S = \mathrm{d}x_b/\mathrm{d}t$ satisfies

$$[h(u-S)] = 0 \quad \text{and} \quad [h(S-u)^2 + gh^2/2] = 0 \tag{13}$$

with $[\cdot]$ the jump in quantities across the bore, e.g. $[h] = h_{x\downarrow x_b} - h_{x\uparrow x_b}$. We analysed simulations of (12), including the bore relations and a wave-maker modelled by prescribing movement of a very steep beach in a limited x–interval and a fixed beach of about 0.5m. They indicate that there is a threshold for which the bores generated are strong enough to travel across the beach for a lateral tank width of crica $2l = 1.5$mm and wave frequencies between 0.5–1Hz. For smaller gap widths $2l < 1.5$mm the bores generated die out too quickly due to the Newtonian momentum damping in the width- and depth-averaged equations (12). Given available and suitable zeolite particles with a diameter of $d = 1.8$mm, the gap width in the experimental design can finally be chosen as $2l = 2$mm. An illustration of such a design simulation is provided in Fig. 3.

2.2 Potential flow model

Given the wave sloshing validation presented later, we assume that the domain consists of solid verticals walls and fixed bottom together with a free surface. The next step is to impose the velocity field to satisfy the potential flow Ansatz $\bar{\boldsymbol{u}} = (\bar{u}, \bar{w}) = \boldsymbol{\nabla}\phi \equiv (\partial_x\phi, \partial_z\phi)$ with velocity potential ϕ. Consequently, the remaining (horizontal) vorticity component $\partial_z\bar{u} - \partial_x\bar{w}$ in (9) is zero. It is therefore convenient to rewrite (9) first as follows

$$\partial_t\bar{u} + \partial_x\big(\frac{1}{2}\gamma(\bar{u}^2 + \bar{w}^2) + P/\rho_0 + gz\big) + \gamma\bar{w}(\partial_z\bar{u} - \partial_x\bar{w}) = -3\nu\bar{u}/l^2, \quad (14a)$$

$$\partial_t\bar{w} + \partial_z\big(\frac{1}{2}\gamma(\bar{u}^2 + \bar{w}^2) + P/\rho_0 + gz\big) - \gamma\bar{u}(\partial_z\bar{u} - \partial_x\bar{w}) = -3\nu\bar{w}/l^2, \quad (14b)$$

$$\partial_x\bar{u} + \partial_z\bar{w} = 0. \quad (14c)$$

Substitution of $\bar{\boldsymbol{u}} = \boldsymbol{\nabla}\phi$ into (14) then yields

$$\partial_t\phi + \frac{1}{2}\gamma|\boldsymbol{\nabla}\phi|^2 + gz + p/\rho_0 + 3\nu\phi/l^2 = K, \quad (15a)$$

$$\nabla^2\phi = 0, \quad (15b)$$

in which K is an integration constant. Evaluation of (15a) at the free surface, where $p = p_0$ is the constant pressure of the passive air, yields the dynamic boundary condition. The integration constant $K = p_0/\rho_0 + gH_0$ is conveniently defined, when the still-water free surface at $z = H_0$ is considered. Combined with the kinematic free surface equation (10a) for $b = 0$ with again $\boldsymbol{u} = \boldsymbol{\nabla}\phi$, the dynamic and kinematic boundary conditions at $z = h$ become

$$\partial_t\phi + \frac{1}{2}\gamma|\boldsymbol{\nabla}\phi|^2 + g(h + b - H_0) + 3\nu\phi/l^2 = 0 \quad (16a)$$

$$\partial_t h + (\partial_x\phi)\partial_x h - \partial_z\phi = 0. \quad (16b)$$

These are used to solve the Laplace's equation (15b), in combination with no normal flow conditions $\hat{\mathbf{n}} \cdot \boldsymbol{\nabla}\phi = 0$ at solid walls, with outward normal $\hat{\mathbf{n}}$.

The first and last term in the dynamic free boundary condition (16a) can be combined in an integrating factor. When denoting evaluation at the free surface by $(\cdot)_s$, these two terms can be written as:

$$\big((\partial_t\phi)_s + 3\nu\phi_s/l^2\big)e^{3\nu t/l^2} = \partial_t(\phi_s e^{3\nu t/l^2}) - (\partial_z\phi)_s(\partial_t h)e^{3\nu t/l^2}, \quad (17)$$

in which we used that $\partial_t(\phi_s) = (\partial_t\phi)_s + (\partial_z\phi)_s\partial_t h$. For a large damping factor $3\nu/l^2$, the potential and kinetic energy will quickly damp out. A relevant extension of Miles' variational principle [21] for water waves based on potential flow then becomes

$$0 = \delta\int_{t_0}^{T}\Bigg(\int_0^L \big(\gamma\phi_s\partial_t h - \frac{1}{2}\gamma g(h - H_0)^2\big)\mathrm{d}x - \int_0^L\int_0^{\gamma h}\frac{1}{2}\gamma|\boldsymbol{\nabla}\phi|^2\mathrm{d}z\mathrm{d}x\Bigg)e^{3\nu t/l^2}\,\mathrm{d}t. \quad (18)$$

At the side walls $x = 0, L$ we use that $\partial_x \phi = 0$, at the flat bottom $z = 0$ that $\partial_z \phi = 0$, and we employ the end-point conditions $\delta h(x, t_0) = \delta h(x, T) = 0$. Variation of (18) with respect to the conjugate variables $\{\gamma h, \phi_s e^{3\nu t/l^2}\}$ at the free surface and ϕ in the interior of the domain, then suggests that it is better to plot a modified potential energy

$$P(t)e^{3\nu t/l^2} \equiv \int_0^L \frac{1}{2}\gamma g(h - H_0)^2 \mathrm{d}x e^{3\nu t/l^2}, \tag{19}$$

instead of $P(t)$ for stronger damping. Even though the kinetic plus potential energy times $e^{3\nu t/l^2}$ is not conserved, $P(t)e^{3\nu t/l^2}$ oscillates around a positive mean value, as we will discuss below, and a modified total energy seems to tend to a constant; both at later times. The reason is that due to the damping, the nonlinear system becomes asymptotically linear at later times, with an energy that is quadratic. The following transformation then removes the explicit time dependence $\tilde{\phi}_s = \phi_s \exp\left(3\nu t/(2l^2)\right), \tilde{\phi} = \phi \exp\left(3\nu t/(2l^2)\right)$ and $\eta = (h - H_0) \exp\left(3\nu t/(2l^2)\right)$. Expressed in these new variables, the variational principle (18) and energy no longer have any explicit time dependence anymore in the long-time limit for which the dynamics becomes linear.

3 Experimental set-up and techniques

The primary Hele-Shaw cell consists of two parallel glass plates of length 960mm and a gap of width $2l = 2$mm. It is partially filled with water to a still-water depth of H_0. The wave-maker at one end of the cell consists of a vertical, double welding rod, made of metal, moving between the two glass plates. Each welding rod has a a diameter of 1.6mm, and a length of $l_{wm} = 333$mm measured from its attachment to the pivot point. The wave-maker is driven by a linear actuator (Copley Controls ThrustTube® , type STC-2506-S), which moves back and forth sinusoidally at a fixed amplitude, for example 30mm, and frequency f_{wm}, causing a sinusoidal motion with angular amplitude, for example $\theta_{\mathrm{wm}} \approx 21°$. The linear actuator is connected to the wave-maker by a metal rod and a spring, which are used to regularize the motion of the linear actuator. It affects a slight deviation between the programmed and measured wave-maker motion. Via an amplifier (Copley Controls Xenus® , type XTL-230-18-S), the linear actuator driving the wave-maker is controlled by a PC. Fig. 4 shows a schematic top view of the set-up. Two Hella® flood lights illuminate the Hele-Shaw cell from behind, diffused by an opaque screen placed directly behind the cell.

Near the middle and at the bottom of the cell, a plastic wedge in the shape of a truncated triangle is placed. It prevents particles interfering with the wave-maker's motion, which could otherwise become blocked. The wedge measures 212mm at the bottom and 20mm at the top, with a height of 50mm.

Three types of experiments are undertaken: (i) short-time wave sloshing experiments without particles in which the free surface motion is measured, (ii)

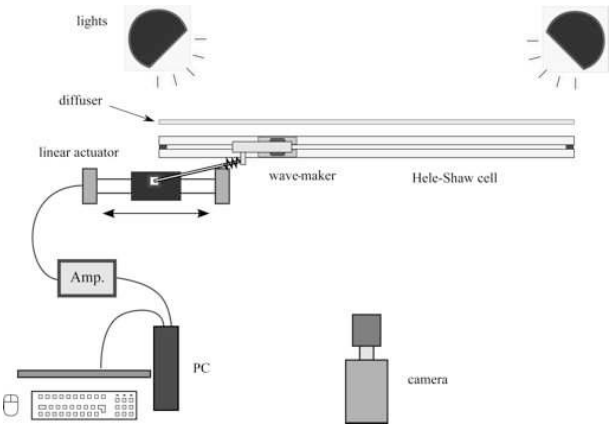

Fig. 4 Schematic top view of the Hele-Shaw experimental set-up.

Material	Diameter (mm)	Density (g/cm^3)	Porosity
Gamma Alumina	1.75 ± 0.1	2.08 ± 0.2*	0.53 ± 0.05
Spherical Glass	1.80 ± 0.1	2.515 ± 0.03	0

Table 1 Properties of particles. *: effective density, with partially water-filled pores.

short-time breaking wave measurements with a bed of movable glass spheres, and (iii) long-time development of quasi-steady beach morphologies with a bed of movable Gamma Alumina particles. Both sets of particles have diameters of around 1.75mm. Further particle properties are provided in Table 1.

3.1 Free-surface wave tracking

In the wave sloshing validations, the high-speed camera used in front of the cell is a Mikrotron Eosens with an Avanar 28 mm lens, recording images at 500fps, and with a shutter time of 1.5ms.

In the wave breaking experiments, taking place on a time scale of one second, details are captured by a high-speed Photron SA2 camera with a 50 mm lens. This enables recording speeds up to and including 1000fps. These experiments involve about 10^4 of movable spherical glass spheres. The wave breaking results are analysed in section 4.

In both cases, 0.2% by volume red dye is added to the water to heighten the contrast between water and air. The presence of the red dye has little discernible effect on the surface tension of water. A programme has been written to accurately extract the free-surface location from the high-speed video frames, making use of the increased contrast. The code is designed such that it can deal with arbitrary wave shapes. Developed in MATLAB, it makes use of its image processing toolbox. The data created are a sequence of three di-

mensional points (x, z, t) that approximately describe a free surface in space and time.

At the start of a measurement series the set-up is flushed with clean MilliQ® water a number of times. Before each measurement, water is drained from or added to the Hele-Shaw cell until the desired water level was reached. In some cases, surfactant was added to the MilliQ® water. In these cases, a known amount of surfactant (Dreft®) is added to the water at first, often further diluted by flushing several times with clean MilliQ® water. The water-air surface tension σ is therefore not exactly the same in all measurements.

3.2 Patch tracking of the bed

Since the experiments concerning the beach morphologies take place on a longer time scale, photographs are taken only every 10s using a Nikon D5100 camera with a Nikon AF Nikkor 50mm lens. A square grid with spacing 20mm was attached to the glass front of the Hele-Shaw cell, photographed, and then removed. This provides a reliable reference for the measurements, and also reveals possible lens distortions in the region of interest. The first photograph of each measurement consists of a rest state. In the 10s between the first and second photograph, the linear actuator is started, linearly accelerating from rest to the desired constant frequency in approximately 2s. Subsequently, the experiment continues till a quasi-steady beach morphology emerges, with little net variation over time. Whether a quasi-steady state is reached, is judged visually. Additionally, a detailed, automated analysis is conducted a-posteriori confirm or revoke the visual assessment of the steadiness of the morphology. At the end of each experiment, camera recording and wave-maker motion are stopped, and the photographs are retrieved.

Snapshots from a typical measurement were shown in Fig. 2, in which the bed evolved from a flat state to a beach with a nearly constant slope. To analyse such beach formation, a patch tracking code has been developed in MATLAB. It determines the location of each particle in each frame, but does not cross-correlate particles locations in consecutive frames. The program has two stages. It first determines the locations of the centres of the bed particles in each frame, using a MATLAB adaptation by [4] of the IDL Particle Tracking software by [14]. Secondly, it determines which bed particles actually belong to the bed surface. Essentially, the zonal x-direction is divided into bins such that the highest particle in each bin is used to define the beach surface.

The surface tension of the water was checked using an OCA apparatus, making use of a pendant drop method to determine the surface tension. These experiments implied a significant change in surface tension within a matter of hours to days. To start each experiment, a set procedure is therefore followed. The particles are placed into the set-up filled with water a day in advance, such that the pores saturate with water. At the beginning of a set, the set-up is flushed a few times with fresh MilliQ® water. It results in a relatively constant surface tension. The beach is levelled and set manually, upon which

its height B_0 is measured. Subsequently, the set-up is drained and refilled with clean MilliQ® , until the water level reaches the desired depth H_0. The water inlet and outlet tube is plugged during the experiment to minimize flow in the tube. As described easlier, the wave-maker motion is controlled by a linear motor. Its horizontal amplitude was fixed at 30mm, and the resulting wave-maker angular motion was 21 ± 1^o from the vertical. The air temperature was not controlled but was monitored carefully. It remained reasonably constant during the experiment, and no noticeable rise in the water temperature was observed. The range in this fixed room temperature was 23.5 to 28.7°C. The properties of water change only slightly with temperature in this range, and the influence on the results seems negligible. The beach morphology experiments are presented in section 5.

3.3 Interim validation

The mathematical design of the Hele-Shaw beach experiments hinged on the simplification of the Navier-Stokes equations with their Newtonian damping into width-averaged Euler equations (14) with linear damping in the momentum equations, or the corresponding potential flow water wave model (16). We have devised an idealized laboratory test to assess quickly to what extent this linear momentum damping is adequately modelling wave dynamics in the Hele-Shaw cell.

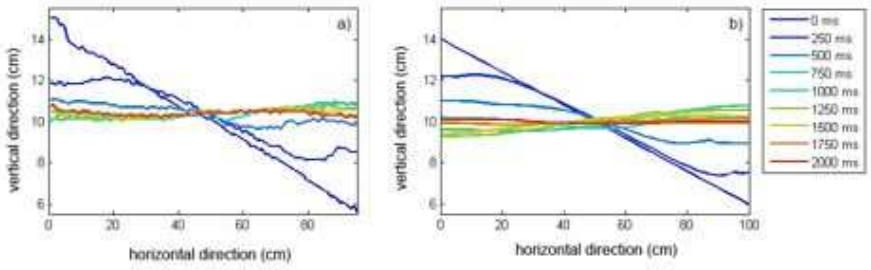

Fig. 5 Free surface profiles in the a) wave sloshing experiment and b) simulation are shown at different times for a tank or free surface initially titled at $\alpha = 4.6$. Time is rearranged such that the first minimum in $P(t)$ coincides for both experiment and simulation.

Simulations of the potential flow model (15b)–(16) derived earlier are therefore compared with laboratory experiments on wave sloshing in the rectangular Hele-Shaw tank, yet without any particles. For the simulations, the initial condition at time $t = t_s$ is one of rest with a free surface uniformly inclined at a small angle α. Such an initial state is difficult or impossible to achieve in the experiments. Instead, for the experiments we have tilted the tank over the same angle α with the fluid at rest. Subsequently, at time $t = t_s - \Delta\tau$

we quickly yet smoothly with minimal impact lower the tank to its horizontal position in a small time interval $\Delta\tau$, such that the motion initiated at $t = t_s$ is minimal. We thus assume that at $t = t_s$ the initial state is approximately the same for the simulations and experiments. The numerical discretization of the water wave model is an extension of the one described in [12], including the algebraic damping term discussed above. It is a (dis)continuous Galerkin finite element model based on a discretization of Miles' [21] variational principle.

To minimize the complexity of the laboratory measurements and guided by the analysis of the potential flow model, we only record snapshots of the free surface. It is particularly illuminating to compare the time evolution of the potential energy $P(t)$ and modified potential energy (19) between experiments and simulations. Such a comparison of the energy as function of time was made for multiple angles α in [7], except for $\alpha = 4.6^{\circ}$. Hence, a more extensive comparison is presented next by looking at the differences between the free surfaces profiles as well as these energies for $\alpha = 4.6^{o}$.

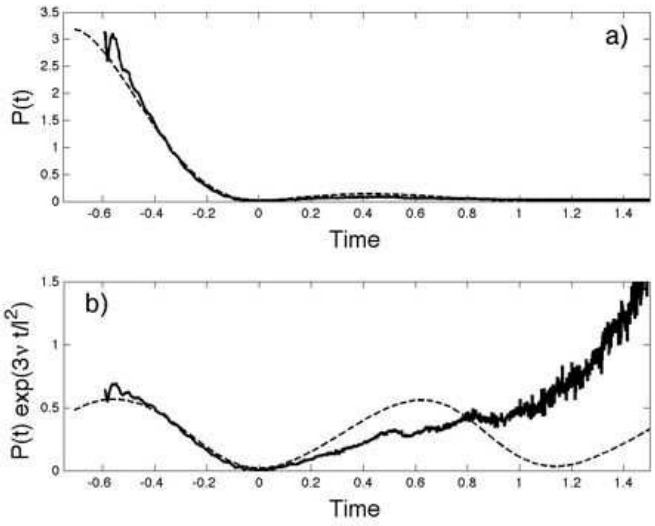

Fig. 6 a) Potential energies $P(t)$ versus time, and b) $P(t)exp(3\nu t/l^2)$ versus time of the measurement (noisy line) and simulation (smooth line) for $\alpha = 4.6^{\circ}$. The time in the simulation is shifted such that $t = 0$ coincides with the first minimum of $P(t)$ in the experiments.

The potential energy $P(t)$ is approximated by binning the integral in a Riemann sum over segments $\Delta x \approx 1$mm, corresponding to the resolution of the camera. Due to light distortion and intrinsic properties of the analysis programmed, small parts of the water surface at the edges of the set-up are not taken into account. This implies that free surface contributions of in total

1cm are neglected near the walls. Given the tank length of $\sim$ 96cm, the error the potential energy calculated is thus approximately 1%.

Snapshots of the free surface are displayed in Fig. 5 for both a) measurements and b) simulations for times $t - t_s = 0, 250, \ldots, 2000$ms. These compare reasonably well, and in both cases a wave reflects off the right wall around times $t_s + 250$ and $t_s + 500$ms. To analyse the differences more accurately, in Fig. 6. a) the potential energy and b) its modified version are shown as function of time. The potential energy $P(t)$ versus t between the two appear appear to match well. The modified potential energy in Fig. 6b) does reveal the differences. For about $0.8s$ the comparison is good, but beyond that time the energy in the measurements is larger. It suggests that the linear momentum damping based on the Poisseuille velocity profile is reasonable for the interior of the fluid, but likely does not work well near the free surface. At the free surface the velocity profile is anticipated to become intrinsically different and surface tension will play a larger role. We also note that the modified potential energy for the simulations is indeed approximately oscillating around a mean, as argued.

The conclusions of our interim validation are as follows. The linear momentum damping used in the mathematical design of the experiment works well for the bulk. However, we have seen that it will be less optimal for fine-scale features at the free surface, such as those observed in the wave breaking results presented next.

4 Breaking waves and bottom slopes

[13] reported four types of breaking waves: spilling, plunging, collapsing and surging breakers. A description of these waves types is given in the review of [23], reproduced in Table 2. These breaker types can be categorized based on the Iribarren number [3], i.e.,

$$I_b = \tan\alpha / \sqrt{H_b/L_b} = T_w \tan\alpha / \sqrt{2\pi\, H_b/g} \tag{20}$$

with the wave period T_w, slope angle α, and breaker wave height H_b. The wave length $L_b = \sqrt{2\pi H/(gT_w^2)}$ is based on linear deep water waves, which does seem striking for the shallow water waves considered. Nonetheless, from spilling, plunging to collapsing and surging breakers, the ordering at real-world beaches is roughly as follows: $I_b < 0.4, 0.4 < I_b < 2.0, 2.0 < I_b < 3.3, I_b > 3.3$. Qualitatively, this ordering ranges from steep waves on mild slopes for spilling breakers, to shallow waves on steep slopes for surging breakers. The question is how these wave breakers and corresponding Iribarren numbers on real world beaches relate to those observed on Hele-Shaw beaches.

Two series of experiments will be analysed, one filmed in the first 0.6m long Hele-Shaw tank (January 2010), and one in the second 0.96m tank (May 2012), discussed sofar. In both experimental series, all four wave types are to a greater or lesser extent observed, with the evidence for the collapsing breaker being the weakest. The four wave breakers in Fig. 7 arise from the first series,

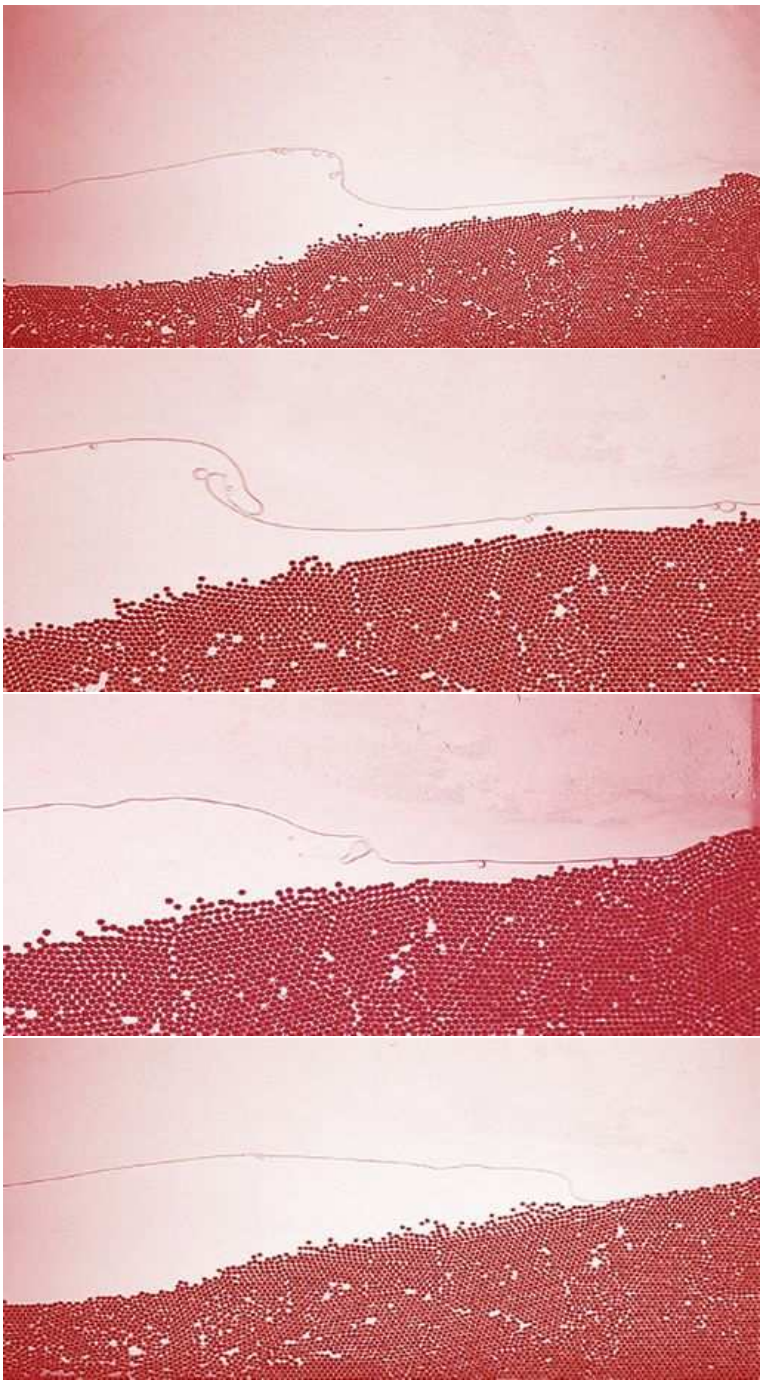

Fig. 7 Top to bottom: still images from spilling, plunging, collapsing and surging breakers (colour enhanced and reversed horizontally for consistency).

Type	**Description**	**Occurrence in cell?**
Spilling	Bubble-rich water appears at wave crest and spills down front face, sometimes proceeded by projection of a small jet	In our case bubbles collect at the face, no new bubbles are generated.
Plunging	Most of wave's front face overturns and a prominent jet falls near the base of the wave, causing a large splash	Yes
Collapsing	Lower portion of front face overturns and behaves like a truncated breaker	The bottom part of the breaker protrudes, but does not plunge.
Surging	No significant disturbance of the smooth wave profile occurs except near the moving shoreline	Yes

Table 2 The definition of the four wave breakers observed in the real world is discussed in relation to breakers in the Hele-Shaw set-up.

Parameter	Value	Parameter	Value
L	857 ± 2 mm	d	2.0 ± 0.05 mm
x_{w}	372 ± 1 mm	l_{w}	212 ± 0.1 mm
h_{w}	5 ± 0.1 mm	t_{w}	20 ± 0.1 mm
x_{wm}	305 ± 2 mm	Δ_{wm}	15 ± 0.5 mm
h_{wm}	337 ± 1 mm	l_{wm}	327 ± 1 mm
θ_{wm}	21°	T	20-25 °C
ρ_b	2.515 ± 0.03 kg dm^{-3}	D_b	1.8 ± 0.1 mm

Table 3 Overview of the parameters fixed in the second series of wave breaking experiments.

and the snapshot of the plunging breakers in Fig. 8 from the second series of measurements.

In the second series of breaking wave experiments, the experimental procedure is as follows. The values of H_0 and f_{wm}were varied per experiment. In contrast to the first series, the beach was manually reordered by trial and error into a shape favouring each type of breaker. The effect of different bottom shapes is thus explored. The camera recording at 1000fps was switched on for a few wave periods, (seconds) after the wave-maker, in about 2s, reached a constant frequency. Subsequently, the recorded images were saved to avoid data overloading. This process was repeated several times for different bed shapes, water levels, wave-maker frequencies and recording speeds. The phenomenology for each wave breaker will be discussed in the following four paragraphs. We recall their definitions from Table 2.

Spilling: In the Hele-Shaw set-up, the spilling breaker is characterised by bubbles accumulating on the crest of the wave. Every cycle, the front face of the wave becomes almost vertical without full breaking. For real-world breakers, white water appears at the wave crest, indicating the presence of many small bubbles, and spills down the front face, sometimes preceded by the projection of a small jet. The observed spilling breakers gather bubbles at the crest, equivalent to the white water of real-world breakers. In contrast, neither bubbles creation is observed at the interface when it is almost vertical, nor the creation of small jets. Pre-existing bubbles are simply advected along by

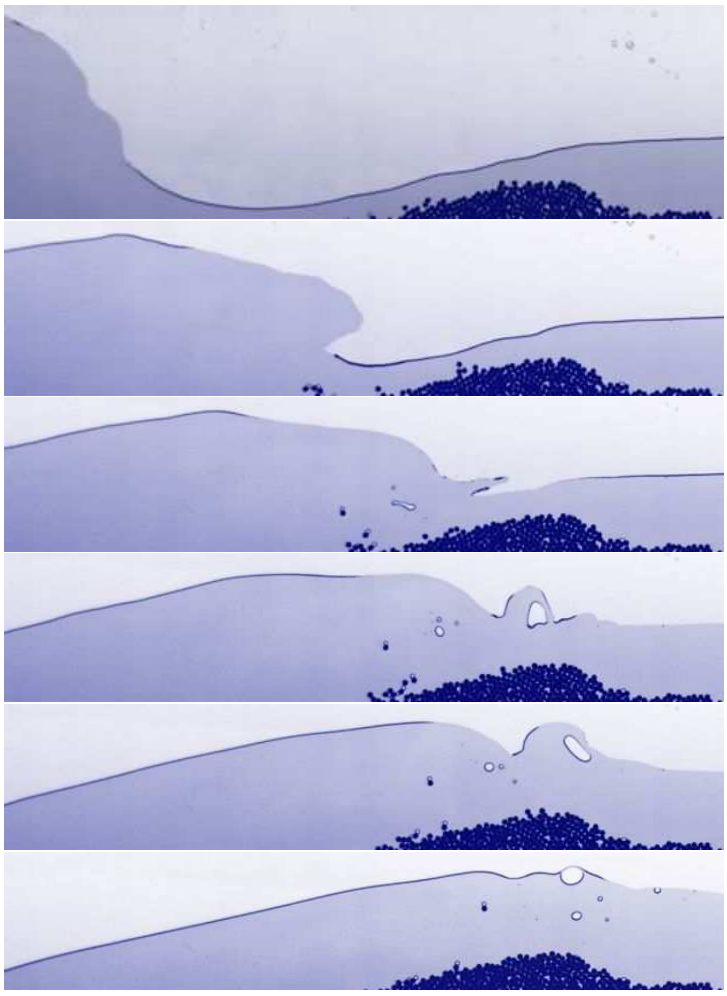

Fig. 8 Sequences of images show the evolution of a Hele-Shaw plunging breaker (colour enhanced). Top to bottom: $t = 100, 150, 200, 250, 350$ms from the initial frame frame. Remarks: initial water level $H_0 = 98 \pm 1$mm and wave-maker frequency $f_{wm} = 1.1$Hz.

a passing Hele-Shaw breaker. We therefore do observe spilling breakers in our Hele-Shaw set-up, but due to the effects of surface tension there are noticeable differences to the real-world counterparts.

Plunging: Snapshots of a plunging breaker are shown in Fig. 8. Firstly, the wave front overturns (second image) creating a jet near the base of the wave (third image), which leads to a large splash (fourth and fifth image). The latter splash entrains a air that creates a bubble, which rises to the surface (sixth image). In doing so, the dynamics in the set-up yields a miniature version of all stages in a real-word plunging breaker.

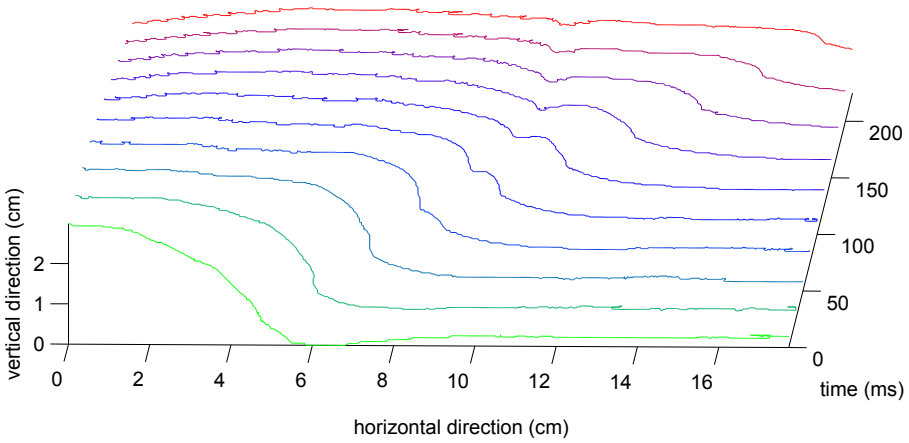

Fig. 9 Free surface profiles of a collapsing breaker. The lines are spaced 25ms apart, denoted in green at early and in red at later stages. Remarks: wave-maker frequency $f_{wm} = 0.9$Hz and initial bed depth $H_0 = 95 \pm 1$mm.

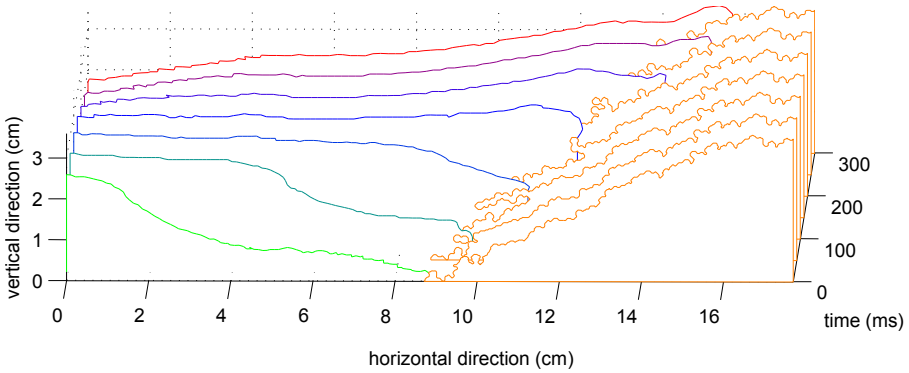

Fig. 10 Waterfall plots are shown for a surging breaker, each 50ms apart. Orange lines indicate the beach location. Remarks: initial beach height $H_0 = 95 \pm 1$mm, wave-maker frequency $f_{wm} = 0.90$Hz and no surfactant is added.

Collapsing: Free surface profiles of a typical collapsing breaker are shown in Fig. 9. This breaker is characterised by splitting of the wave face into an arrested upper part and protruded lower part, which occurs in the time interval $75 - 125$ms. We notice that the wave front is almost vertical just before the collapse at around 50ms. The upper part of the wave is seen to move forward, and upward to a certain point, after which its horizontal position remains nearly constant for about the remaining 100ms displayed in the figure. This may be caused by the two contact lines of the breaker at the glass surfaces. Although the collapsing breaker does show truncation of the practically vertical front face, the lower portion has not been observed to plunge, in contrast to collapsing breakers in the real-world.

Surging: The behaviour of a typical surging breaker observed on the Hele-Shaw beach follows from the water and bed surface profiles versus time in Fig. 10. Hardly anything happens to the wave after 100, till the time reaches the shore at about 150ms. Then, it suddenly overturns and runs up the shore from 150 to 300m, reaches its highest point, after which point it recedes back (not shown). This surging breaker moves a lot of particulate matter in the very shallow water near the shore. The description of a surging breaker at real-world beaches corresponds remarkably well with our observations in the Hele-Shaw set-up.

4.1 Iribarren number

Wave breaking in the first experimental series was filmed with a standard video camera recording at 50fps during various stages of beach formation. The bottom slope comprised of the zeolite or Gamma Alumina particles evolved naturally due to the wave action. A manual determination using an onscreen ruler and protractor of the wave height H (trough to crest) and a mean bottom slope α near wave breaking reveals the following[1]. A definite beach slope is difficult to define clearly in the zone where the wave breaks or starts to break. The corresponding estimated values $\alpha = 22, 27, 29, 26^o$ of the beach slope For the ordering from surging, collapsing, plunging to spilling breakers, respectively, are therefore prone to contain larger errors. The maximum wave heights $H = 4.2, 4.0, 3.8, 6.0$cm as measured in the relevant video frames are more accurate, as are the wave periods $T = 1.1, 0.8, 0.8$ and 0.8s, respectively. Finally, the corresponding Iribarren numbers are $I_b = 1.9, I_b = 1.7, I_b = 1.6$ and $I_b = 0.8$ for surging, collapsing, plunging and spilling breakers on the Hele-Shaw beach.

Concerning the second experimental series, all four types of breakers observed on the Hele-Shaw beach lead to a net particle transport, and therefore evolution of the bathymetry. The time scale of this evolution is longer, on the order of minutes to an hour, than the time scale of the waves, which are on the order of one half to one-and-a half second. As expected, changes in the bathymetry have a strong feedback effect on the wave dynamics, often leading to a change of breaker type. It is clear from the still photos shown in Fig. 7 that the bathymetry is different for each wave breaker. For the second series, it was not possible to extract the bottom profiles and extract the respective Iribarren numbers, due to the nature the measurements were set up. We observe that: (i) the surging breaker occurs on a beach with two distinct angles; (ii) the collapsing breaker occurs in a beach with a submerged sand-bar (the small elevation under the vertical section of the wave profile); (iii) the plunging breaker is generated over a steep shallow section of the beach, whereas (iv) the spilling breaker rolls over a gently rising bathymetry. Note that these

[1] The source file *golfbakonno2.avi* contains surging, collapsing, plunging and spilling breakers at $8, 133, 115$ and 63s, respectively.

qualifications correspond roughly to to real-world situations, in which surging breakers are often long, low waves over steep bathymetry, while spilling breakers concern steep waves over mildly sloping bathymetry.

We summarize the movement of the bed particles observed in both measurement series. Broadly speaking, the plunging breaker moves a great deal of material onto the steep section of the beach; the collapsing breaker moves material from the apex of the submerged sand bar onshore; the spilling breaker is moving material all along the length of the bathymetry; and, finally, the surging breaker is moving material at the break in the bathymetric slope. The trend seems to be that most material is entrained by the wave when the depth is shallow and at locations where there is a change in shape of the bathymetry.

5 Quasi-steady beach morphologies

The nature of the viscous damping in the configuration has been analysed thus far. Consequently, we showed experimentally that all wave breakers are present in idealized form. Our next step is to demonstrate systematically how beaches and berms in the Hele-Shaw cell are formed by breaking waves.

In total 80 measurements were performed to cover the parameter space spanned by wave-maker frequency $f_{wm} \in [0.6, 1.4]$Hz, and the initially quiescent bed and water levels $B_0 \in [3, 8]$cm and $W_0 = H_0 - B_0 \in [1, 8]$cm. All measurements were performed in a semi-random order. This ensured that unforeseen variations of parameters not varied purposely, did not coincide with a gradual variation of the three parameters we did vary systematically. Since adding and removing particles to and from the tank is a slow process, mainly due to the porosity of the Gamma Alumina particles, measurements for each beach height B_0 were performed successively. However, the order in which W_0 and f_{wm} was varied was random. The results obtained are reproducible for two reasons: the phase diagram presented below shows a coherence that would otherwise be absent, and a total of five measurements has been repeated, essentially yielding the same outcomes.

Quasi-steady state beach morphologies emerge on a timescale of minutes to an hour. On this timescale, wave motion is changed in nature in response to the changing bed forms. Initially the bed is flat, except near the wedge, and the waves may not break. Once the water depth becomes shallower, in the course of time, wave breaking generally sets in or becomes more pronounced. In most cases, the particles of the bed keep moving during the monochromatic wave cycles, so the beach morphology is quasi-steady not steady. While the experiments are terminated when the experimentalist judges the state to be quasi-steady, an extensive and automated analysis is performed a posteriori. This analysis is based on the patch tracking algorithm outlined earlier.

The extensive sediment transport analysis undertaken to establish whether the bed morphology has become quasi-steady is outlined, as follows. The difference between the initial state and an evolved state consists of a negative area of moved sediment and a positive area of deposited sediment. These areas

do not quite coincide because the deposited area has a larger compaction of a few percent. An effective distance travelled by the sediment is represented by the distance between the centres of mass of these areas. This evolves over time. The bed state can now be described adequately by the cubical transport, being the product of the (negative) sediment area times the effective distance the sediment travelled. The time derivative thereof yields a cubical transport rate, for which the wave-maker period T_{per} is used as the relevant time unit. Finally, a bed is confirmed as quasi-steady when this cubical transport rate falls below a threshold of $100\mathrm{mm}^3/\mathrm{T}_{\mathrm{per}}$. That rate corresponds roughly with 3 bed particles being transported over a distance of 1cm per wave-maker period. More information on the sediment analysis is found in [16].

An overview of the observed quasi-steady bed morphologies is presented in Fig. 11, which shows for each morphology the initial quiescent (red lines) and final quasi-steady state of the bed. Although the transition between the morphologies is smooth, a mathematical classification can be based on the minimum and maximum extrema of the bed profile of this quasi-steady state. A quasi-steady state is deemed to be dry if at least one onshore particle at the bed surface remains dry. A swash zone emerges when the bed intermittently breaks the free surface and is alternately wet and dry when the waves run up and down the beach. Due to the interaction with the dynamic bed, some waves are slightly higher than others, even in the quasi-steady phase, such that an extra particle can be swung up the beach or dune. This particle at the top is nearly always totally dry, or dry on top, or dry on the offshore side if it lies freely at the summit unsupported by the wall. When there is a maximum, it is thus either dry or wet, in the interior or at the boundary. A berm or dune has a dry interior maximum or island, with water on either side (Fig. 11(a)). A dune-beach has a dry interior maximum with land on the onshore side (Fig. 11b). A submerged sandbar has a wet interior maximum (Fig. 11(c)). A dry or wet beach is a state with a boundary maximum (Fig. 11(d,e)). Sometimes nearly no transport occurs because the water is too deep, giving a quasi-static state (Fig. 11(f)). Finally, in a suction state particles disappear over the wedge due to the action of the wave-maker (Fig. 11(g)), with a flat quasi-static part onshore and an interior or boundary minimum near the wedge. This interference inhibits the wave-maker such that the experiment must be halted. A suction state is also inferred, when more than 90 particles disappear from the bed by crossing the wedge within 20min of the bed evolution.

All quasi-steady bed morphologies in the experiment are displayed in Fig. 12 based on an automated image analysis (MATLAB) and the classification outlined above. Qualitatively, the following patterns emerge. Dunes emerge when the initial still water depth is shallow, $W_0 \approx 1$cm, followed by dune-beaches, dry beaches and wet beaches at $3, 5, 7$cm initial depths, respectively. The evolution of several quasi-steady bed morphologies is discussed next.

Typical *berm or dune* formation starts with an initial heap of newly-transported sediment that is formed just behind the wedge (Fig. 13a)). Subsequently, this particle mass starts moving towards the shore and grows, until at some point it breaks through the free surface. Because the water depth

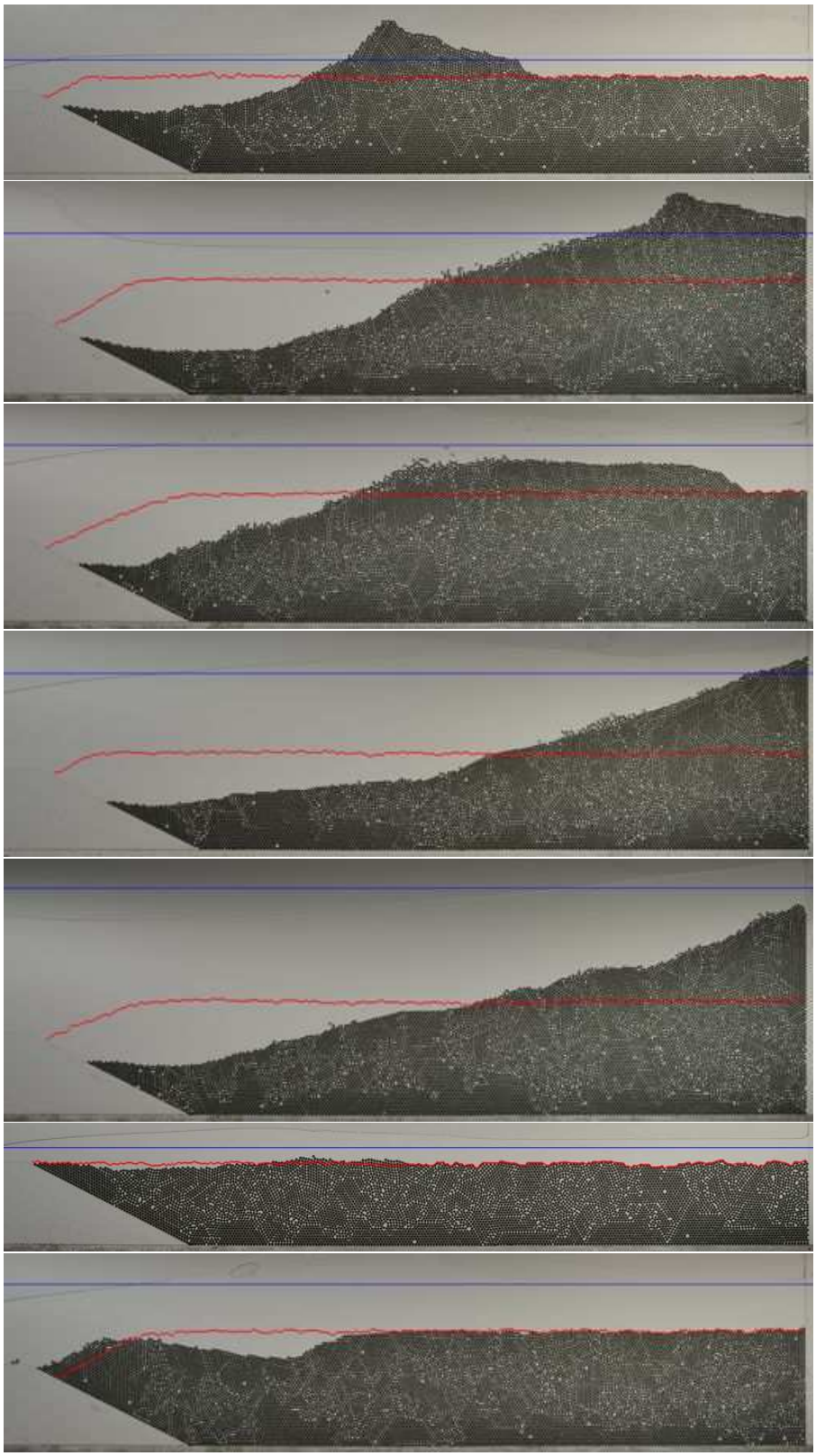

Fig. 11 Photos of quasi-steady bed morphologies and corresponding initial states leading to a classification based on the extrema identified: a minimum or maximum in the interior or the boundary of the bed. Red lines indicate initial bathymetries and blue lines initial water levels. From top to bottom the states are: a dune and dune-beach (dry interior maxima) and a submerged sand-bar (wet interior maximum); a dry and wet beach (boundary maxima); quasi-static (less than 10cm^2 displaced sediment area); and, one of suction (interior or boundary minimum with onshore quasi-static part).

SBM	Definition	Quantification
dry beach	beach on onshore side	dry maximum at boundary/wall
wet beach	beach on onshore side	wet maximum at boundary/wall
dune	island formation	dry interior maximum, water on either side
dune-beach	dry beach with dune	dry interior maximum with dry land beyond
wet sand-bar	no dry bed parts	wet interior maxium
quasi-static	sediment transport small	wet state: $< 10\text{cm}^2$ replaced sediment
suction	particles sucked to wave-maker region	interior/boundary minimum with largely quasi-static bed

Table 4 A classification is given of steady bed morphologies in the Hele-Shaw cell.

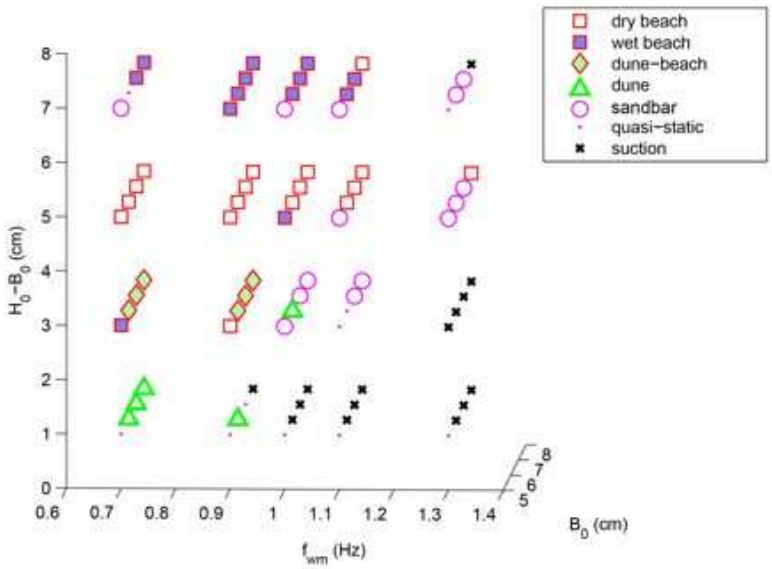

Fig. 12 Phase diagram of all the states as a function of $W_0 = H_0 - B_0$, f_{wm} and B_0.

is so shallow, it induces sufficiently heavy wave breaking, with corresponding dissipation of energy, that further onshore sediment transport is arrested. A berm or dune is formed with wave breaking on its active shore and a calm lake on the other side. Due to the porous structure of the bed, the water level of the lake moves slightly up and down.

Beaches form when the initial water level is deeper (Fig. 13d)). The particle accumulation generated early in the evolution travels to the wall, and keeps growing until a maximum, stable beach angle is reached. The initial dip in the angle is caused by the fact that a particle mass travelling downstream causes a negative slope in the downstream part of the bed just before it reaches the

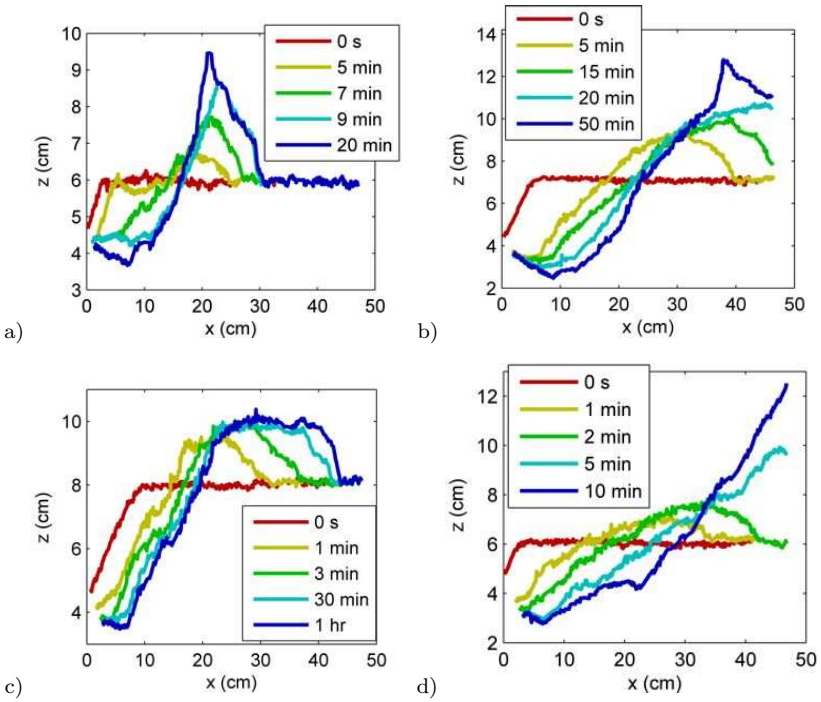

Fig. 13 The formation of a quasi-steady: a) berm or dune, b) dune-beach, c) sandbar, all having an interior maximum; and, d) beach, having a boundary maximum, over time.

end. Sometimes, the water layer is shallow enough for the beach to emerge from the water, constituting a dry beach. When the water layer is too deep, the beach stays submerged and wet, because there are insufficient particles available to form a stable dry beach.

A *dune-beach* appears as a transitional form between the beach and dune regions of the parameter space. The bed evolves like the dry beach case, but once it reaches the water surface it switches to a dune-like evolution, giving a rising bed on the onshore side, leading to the formation of a sharp cliff (Fig. 13b).

Suction states are clearly grouped in the part of parameter space where the frequency is high and the water depth is low. In the suction case, strong offshore sediment transport occurs. Hence, the suction part of parameter space is separated from the beach and dune states by the quasi-static and sand-bar bed morphologies. In the latter two cases, onshore and offshore forces on the bed appear to more balanced, leading to no or reduced sediment transport.

5.1 Bed activity and beach angles

The free water layer depth, W_0, proves to be the most dominant parameter to determine the type of steady bed morphology. Dunes are observed at small

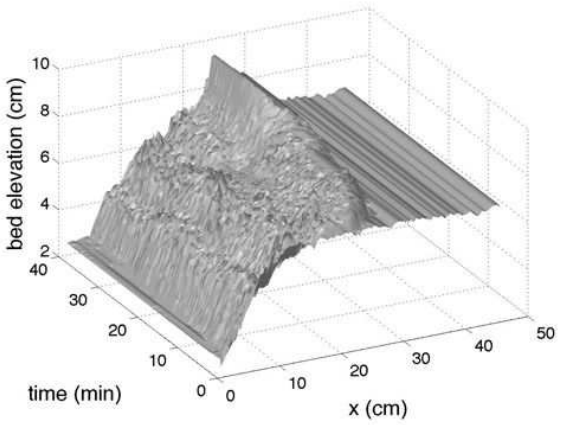

Fig. 14 Dune evolution is displayed as a three-dimensional space-time landscape.

water layer depths around 1cm, beaches at larger depths of about 5cm, and a hybrid dune-beach at an intermediate water layer depth of 3cm. The general activity of the bed is determined by f_{wm} and B_0. When $B_0 = 5$cm, enough sediment is transported to form beaches in only a few cases, while no dunes or dune-beaches are observed. Suction only occurs in one case. For higher initial bed heights B_0, dunes and dune-beaches are formed and more beaches are created, but more instances of suction also occur. Hence, an increase in bed activity emerges with increasing initial bed height. We note that the height 5cm of the fixed wedge between wave-maker and bed correlates with the most pronounced jump in bed activity. Concerning the wave-maker frequency, especially the measurements at $B_0 = 5$ and 7 cm suggest a slight optimum in terms of transport at an f_{wm} of approximately 0.9Hz. We note that the observed bed morphologies are quite reproducible: the phase diagram 12 is coherent.

It is currently unknown what affect the onshore wall of the set-up has onthe results. It is clear that beaches, both wet and dry, are formed when the waves can reach the end of the Hele-Shaw cell without dissipating their wave energy beforehand. Whether or not beaches would alter to dunes in longer set-ups remains unclear, because energy dissipation due to wave breaking and due to side-wall friction are competing effects.

In the beach state, the final, mean and stable slope differs per case. All stable angles are lower than the theoretical angle of repose for (wet and dry) monodisperse circles reported by [1]. Most stable angles lie between 10° and 20°, much lower than the 24±1° for disks reported in [9], and the $\sim 22°$ found for glass and polystyrene beads in [1]. Completely wet slopes are less stable than slopes which are alternatingly wet and dry [24], i.e., the part of the beach in the swash zone. Beach slopes in the swash zone are therefore steeper than the fully wet slopes of the beach. We also observe such a change in the Hele-Shaw cell: the slope in the dune-beach in Fig. 13 clearly increases suddenly at

the foot of the cliff that appears to mark the start of the swash zone. Such a sudden change in slope is less visible in Fig. 13, but the slope at 20min might not have been fully developed. A sudden change of slopes between wet beach and cliff is clearly visible for $t > 20$min for another dune state, displayed in Fig. 14.

6 Conclusions and discussion

We presented the mathematical design of a Hele-Shaw cell for the study of bed dynamics by breaking waves. The design shows that damping can be controlled by calculating the gap width of the cell such that driven nonlinear wave motion survives across the tank, while also retaining the advantages of being nearly two-dimensional, and of having very tractable dynamics.

We thus showed that all types of real-world wave breakers were also observable on the Hele-Shaw beaches in the laboratory, albeit in idealized forms due to the effects of surface tension. In one of the measurements series, the spilling breaker was difficult to identify, and in the other the collapsing breaker was more problematic. Moreover, the Iribarren numbers were estimated from one of the series, showing the right ordering but different values than found on real-world beaches. Finally, a comprehensive parameter study of quasi-steady bed morphologies revealed definite trends in the parameters varied: the levels of the initially flat bed and water at-rest, together with the wave-maker frequency. We could thus identify distinct states at longer times in the bed evolution, such as berms/dunes and beach-dunes, dry and wet beaches, and sandbars.

More work is required to relate wave breaking to the bed shape underneath, and relate that to the Iribarren number. Further investigation to assess the role of the wedge (used for technical reasons in the present study), the role of the length and width of the tank, and the role of the wave-maker is also desirable. A more elaborate video capturing system, such that the fast wave motion can (intermittently) be recorded alongside the recording of the natural long-time bed evolution, would be of value.

There are numerous and sensible variations to be made on the laboratory work. These include study of Hele-Shaw beach dynamics under a systematic increase of the gap width to a few particle diameters, and varying the material properties; such as particle properties (size, shape, and density), liquid properties (alcohol-water mixtures), and the effects of glass coatings (to reduce contact line effects)

In addition, we presented two preliminary models to enable and assess the mathematical design. Further research is required to extend these models to include the multiphase dynamics observed in the Hele-Shaw cell, in a more or less detailed or averaged manner. The advantage of the Hele-Shaw configuration remains that the quasi-two-dimensional nature of the set-up in principle allows the formulation, study and experimental validation of a hierarchy of models. These can range from the Navier-Stokes equations with explicit par-

ticle dynamics for brute-force calculations, to multiphase continuum models and their wave-, width- and depth-averaged versions. Finally, our Hele-Shaw methodology appears useful for benchmarking current wave and sediment forecast models used in coastal engineering [22].

References

1. Albert, R., Albert I., Hornbaker, D., Schiffer P., Barabási, A.-L. 1997: Maximum angle of stability in wet and dry spherical granular media. *Physical Review E* **56**, 6271–6274
2. Batchelor, G.K. 1967: *An Introduction to Fluid Dynamics.* Cambridge University Press. 635 pp.
3. Battjes, J. 1974: Surf similarity. Proc. 14^{rmth} Coastal Eng. Conf., Copenhagen, Denmark, 466–480
4. Blair, D., Dufresne, E. 2012: Matlab Particle Tracking. http://physics.georgetown.edu/matlab/
5. Bokhove, O., Zwart, V., Haveman, M.J., 2010: *Fluid Fascinations.* Publication of Stichting Qua Art Qua Science, University of Twente, Enschede, The Netherlands. The Hele-Shaw experiment was first revealed in a Qua Art Qua Science lecture of O.B. and Valerie Zwart with W.Z. on January 17^{th} 2010, in a tribute to the late Howell Peregrine. http://eprints.eemcs.utwente.nl/17393/
6. Bokhove, O., Van der Horn, A., Van der Meer, D., Zweers, W, Thornton, A.R. 2012: Breaking waves on a dynamic Hele-Shaw beach. Proc. Thirrd Int. Symposium on Shallow Flows. http://eprints.eemcs.utwente.nl/21539/
7. Bokhove, O., Van der Horn, A.J., Van der Meer, D., E. Gagarina and Zweers, W., Thornton, A.R. 2013: Revisiting Hele-Shaw Dynamics to better understand beach evolution. Submitted
8. Calantoni, J. Puleo, J.A., Holland, K.T. 2006: Simulation of sediment motions using a discrete particle model in the inner surf and swash-zones. *Cont. Shelf Res. 26*, 1987–2001
9. F. Cantelaube, F., Limon-Duparcmeur, Y., Bideau, D., G.H. Ristow, G.H. 1995: Geometrical Analysis of Avalanches in a 2D Drum. *Journal de Physique (France)* **5**, 581–596
10. Cotter, C., Bokhove, O. 2010: Water wave model with accurate dispersion and vertical vorticity. *Peregrine Commemorative Issue J. Eng. Maths.* **67**, 33–54
11. Garnier, R., Dodd, N., Falquez, A., Calvete, D. 2010: Mechanisms controlling crescentic bar amplitude. *J. Geophys. Res.* **115**, F02007
12. Gagarina, E., Van der Vegt, J.J.W., Ambati, V.R., Bokhove O. 2012: A Hamiltonian Boussinesq model with horizontally sheared currents. Third Int. Symp. on Shallow Flows Proc. June 4-6, Iowa, http://eprints.eemcs.utwente.nl/21540
13. Galvin, C.J. 1968: Breaker type classification on three laboratory beaches. *J. Geophys. Res.*, **73**, 3651–3659

14. Grier, D., Crocker, J., Weeks, E. 2012: Particle Tracking using IDL. http://www.physics.emory.edu/ weeks/idl/, http://www.physics.emory.edu/ weeks/idl/
15. Grimshaw, R., Osaisai, E. 2013: Modelling the effect of bottom sediment on beach profiles and wave set-up. *Ocean Modelling* **59–60**, 24–30
16. Horn, van der, A.J. 2012: Beach Evolution and Wave Dynamics in a Hele-Shaw Geometry. M.Sc. Thesis, Department of Physics, University of Twente
21. Miles, J. 1977: On Hamilton's principle for surface waves. *J. Fluid. Mech.* **27**, 395–397
18. Lamb, H. 1993: Hydrodynamics. Cambridge University Press.
19. Lane, E.M., Restrepo, J.M. 2007: Shoreface-connected ridges under the action of waves and currents. *J. Fluid Mech.* **582**, 23–52
20. McCall, R.T., van Thiel de Vries, J.S.M., Plant, N.G., van Dongeren, A.R., Roelvink, J.A., Thompson, D.M., Reniers, A.J.H.M. 2010: Two-dimensional time dependent hurricane overwash and erosion modeling at Rosa Island. *Coastal. Eng.* **57**, 668–683
21. Miles, J. 1977: On Hamilton's principle for surface waves. *J. Fluid Mech.* **83**, 153–158
22. Operational forecasting models 2013: Delft3D. Software platform including morphology of Deltares, The Netherlands: http://www.deltaressystems.com/hydro/product/621497/delft3d-suite
Open Telemac-Mascaret: http://www.opentelemac.org/
XBeach: http://oss.deltares.nl/web/xbeach/
23. Peregrine, D.H. 1983: Breaking waves on beaches. *Ann. Rev. Fluid Mech.* **15**, 149–178
24. Roelvink, D., Reniers, A., van Dongeren, A., van Thiel de Vries, J., McCall, R., Lescinkski, J. 2009: Modelling storm impacts on beaches, dunes and barrier islands. *Coastal Eng.* **56**, 1133–1152
25. Rosenhead, L. (ed.) 1963: *Boundary layer theory.* University Press Oxford. 688 pp.
26. Soulsby, R. 1997: *Dynamics of Marine Sands.* In: HR Wallingford. Thomas Telford. 249 pp.
27. Wilson, S.K., Duffy, B.R. 1998: On lubrication with comparable viscous and inertia forces. *Q.J. Mech. Appl. Math.* **51**, 105–124